Accepted Manuscript

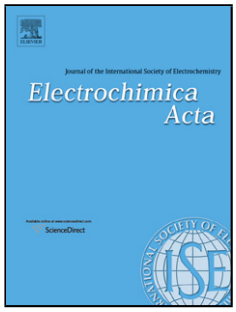

Title: Amorphous carbon thin film electrodes with intrinsic Pt-gradient for hydrogen peroxide detection

Authors: Noora Isoaho, Niklas Wester, Emilia Peltola, Leena-Sisko Johansson, Ana Boronat, Jari Koskinen, Juan Feliu, Victor Climent, Tomi Laurila

PII: S0013-4686(17)31751-6
DOI: http://dx.doi.org/10.1016/j.electacta.2017.08.110
Reference: EA 30114

To appear in: *Electrochimica Acta*

Received date: 24-5-2017
Revised date: 17-8-2017
Accepted date: 17-8-2017

Please cite this article as: Noora Isoaho, Niklas Wester, Emilia Peltola, Leena-Sisko Johansson, Ana Boronat, Jari Koskinen, Juan Feliu, Victor Climent, Tomi Laurila, Amorphous carbon thin film electrodes with intrinsic Pt-gradient for hydrogen peroxide detection, Electrochimica Actahttp://dx.doi.org/10.1016/j.electacta.2017.08.110

Amorphous Carbon Thin Film Electrodes with Intrinsic Pt-gradient for Hydrogen Peroxide Detection

Noora Isoaho[a], Niklas Wester[b], Emilia Peltola[a], Leena-Sisko Johansson[c], Ana Boronat[d], Jari Koskinen[b], Juan Feliu[d], Victor Climent[d], and Tomi Laurila[a]*

[a] Department of Electrical Engineering and Automation, School of Electrical Engineering, Aalto University, PO Box 13500, 00076 Aalto, Finland

[b] Department Chemistry and Materials Science and Engineering, School of Chemical Technology, Aalto University, PO Box 16200, 00076 Aalto, Finland

[c] Department of Bioprocess and Biosystems, School of Chemical Technology, Aalto University, PO Box 16300, 00076 Aalto, Finland

[d] Instituto de Electroquímica, Universidad de Alicante, Apt. 99, 03080 Alicante, Spain

[*]Corresponding author: tomi.laurila@aalto.fi, +358 50 341 4375

Abstract

Nanoscale amorphous carbon thin films with intrinsic Pt gradient show great promise as new electrode materials for electrochemical detection of hydrogen peroxide. Embedding the Pt particles in the carbon matrix during the fabrication process allows tighter integration than, for example, adding them after the fabrication on top of the substrate. Especially, ~~they~~ this approach can offer excellent electrochemical properties combined with CMOS compatibility, which is crucial for further device development. Here we provide extensive in depth electrochemical and

physicochemical characterization of these novel materials by cyclic voltammetry (CV), chronoamperometry (CA), rotating disk electrode (RDE) experiments, transmission electron microscopy (TEM), Raman spectroscopy, x-ray photoelectron spectroscopy (XPS) and atomic force microscopy (AFM). Equipped with these detailed results on these materials we proceed to present some suggestions how the physicochemical properties correlate with the results from electrochemical measurements. (i) It is shown that coarsening of the initially very finely dispersed structure occurs both under electron bombardment during TEM imaging as well as during cyclic voltammetry in H_2SO_4. (ii) Further, it is shown that OH is adsorbed on small Pt islands much more strongly compared to the bulk Pt, which may heavily influence hydrogen peroxide redox reactions on these Pt-containing amorphous carbon films. (iii) Finally, we proceed to demonstrate that despite these complications, these materials show linear response for hydrogen peroxide reduction in neutral phosphate buffered saline combined with very fast response times.

Keywords: carbon, thin films, platinum, sensors, hydrogen peroxide

1. Introduction

Hydrogen peroxide (H_2O_2) is a simple molecule with a high standard electrochemical potential [1] making it a powerful oxidizing agent on appropriate substrates. H_2O_2 has been proposed to be formed as a reaction intermediate in the oxygen reduction reaction [2–4] which makes it an interesting species for fuel cell research and development. In living organisms, cells produce H_2O_2 in the mitochondria to control growth and apoptosis and it might also have a key role in aging [5]. Some tumor cell lines have been suggested to be able to produce large amounts of H_2O_2 in vivo which could, for example, enhance their invasion and metastasis formation [6]. Moreover, endogenous H_2O_2 can inhibit dopamine release and have a role in the etiology of neurodegenerative

disorders, such as Parkinson's disease [7]. Several oxidative enzymes such as glucose oxidase [8], glutamate oxidase [9], and cholesterol oxidase [10] produce H_2O_2 allowing the indirect electrochemical detection of their otherwise electroinactive substrate molecules. Thus, sensors for H_2O_2 detection are in demand in not only industrial but also various healthcare related applications.

Electrochemical sensors are utilized in the detection of various analytes owing to their scalable size and good temporal resolution. Noble metals, such as platinum, gold and silver, as well as their alloys, show good catalytic activity towards H_2O_2 oxidation and reduction [11–17]. Especially the mechanism for electrochemical oxidation of H_2O_2 on Pt has been studied widely by Hall, Khudaish and Hart [18–22]. Also, both H_2O_2 reduction and oxidation on polycrystalline Pt have been studied by Katsounaros et al.[23]

Diamond-like carbon (DLC) is a carbon allotrope with high sp^3 content. The DLC family consist of amorphous carbons (a-C) and their hydrogenated alloys.[24] Tetrahedral amorphous carbon (ta-C) is the form of DLC with the highest sp^3 fraction[25]. In addition to low surface roughness [26], ta-C has good electrochemical properties, such as large water window and low background signal [27], making it suitable for sensor applications. We have previously shown that Pt can be alloyed with ta-C film to form an amorphous carbon (a-C) thin film with an intrinsic Pt islands distribution and that these thin film electrodes can detect H_2O_2 [28]. Furthermore, we showed that GluOx can be immobilized on these carbon thin film surfaces enabling the detection of glutamate [29]. Embedding Pt into the carbon matrix instead of depositing the particles on top of the substrate provides more tight integration, which can enhance the electrochemical properties. Moreover, this approach provides CMOS compatibility, which is especially important for device fabrication. Despite these initial successful steps with sensor applications, basic structural, chemical and electrochemical properties of these new materials are not unambiguously known at the moment. Especially the evolution of various structural nanosized features during electrochemical measurements and their implications to the electrochemical behavior of the materials have not been

previously addressed. Hence, here we investigate in detail the electrochemical properties of a-C/Pt electrodes by utilizing cyclic voltammetry (CV), chronoamperometry (CA) and rotating disk electrode (RDE) experiments. We also present in depth characterization of these films by TEM, Raman spectroscopy, XPS and AFM as well as provide some insight about the correlations of these properties with the observed electrochemical behavior.

2. Experimental

2.1.Sample Preparation

Samples consisted of 20 nm thick underlying titanium layer and approximately 7 nm thick a-C layer gradient-alloyed with Pt. Samples with only an 8 nm thick Pt layer were fabricated as controls. Substrates were highly conductive p-type boron-doped (100) Si wafers with 0.001–0.002 Ωcm resistivity (Ultrasil, USA) or NaCl crystals (Ted Paella, Inc., USA) without Ti layer for TEM sample fabrication. Si wafers were cleaned by standard RCA-cleaning procedure before deposition.

Sample fabrication procedure consisted of direct current magnetron sputtering (DC-MS) for Ti layer and dual filtered cathodic vacuum arc (FCVA) deposition for carbon and platinum layers. Both deposition systems were installed in one chamber. The DC-MS system was equipped with a circular, water-cooled magnetron sputtering source with 2 inch Ti target. Ti layers were deposited to enhance adhesion under the following deposition conditions: discharge power was fixed at 100 W, total pressure was 0.67 Pa, Ar gas flow rate was 29 sccm, deposition temperature was close to room temperature, and deposition time was 350 s. Cathodic arc deposition system (Lawrence Berkeley National Laboratory, USA) was equipped with a 45^{o} bent magnetic filter for reduction of macroparticle contamination and two cathodes in a dual cathode configuration. The cathodes were 6.35 mm 99.95 % purity graphite (Goodfellow) and 99.99 % purity Pt rods (Goodfellow). A pulse

forming network (PFN) was used to strike the triggerless arc. The PFN was controlled with custom made National Instruments hardware and LabView software. To obtain Pt-doped a-C the following functions were used to control the number of pulses for carbon and Pt:

$$C: 50 - 0.5x^2 \qquad Pt: 1 + 0.5x^2 \qquad 0 \leq x \leq 9, x \in Z$$

resulting in a total of 360 pulses of carbon and 155 pulses of Pt. The functions were chosen so that on each cycle the number of carbon pulses decreases and Pt increases, giving a surface with high Pt content.

The arc current pulses had an amplitude of 0.7 kA and 0.6 ms pulse width. During the deposition, the 2.6 mF capacitor bank was charged to 400 V and pulse frequency was 1 Hz. Total pressure during the deposition process was no more than 1.3×10^{-4} Pa. The distance between the substrate holder and the filter was about 20 cm. During the depositions, the samples were at floating potential and rotation was used to ensure homogeneous film deposition (rotational velocity 20 rpm).

After deposition, the wafers were cut into rectangular chips with an automated dicing saw. Samples were stored dry at room temperature. Before electrochemical characterization and H_2O_2 experiments, circular area was defined from the sample with PTFE tape (Irpola Oy, Finland).

2.2. Physical Characterization

The sample morphology was studied with high-resolution transmission electron microscopy (HRTEM) and scanning probe microscopy (Ntegra Aura, NT-MDT Company, Russia). HRTEM was performed with Technai F20 operated at 200 kV. The samples deposited on the NaCl crystals were dissolved in water and subsequently deposited on TEM grids. Scanning probe microscopy, operated in ambient atmosphere, was used for atomic force microscopy (AFM). The measurements were carried out in 'scanning by sample' mode in contact mode with a Si tip (NSG01, NT-MDT

Company, Russia) which had typical curvature and typical force constant of 6 nm and 5.1 N/m, respectively. Obtained topography maps were processed with Matlab.

Visible Raman spectroscopy for the ta-C and Pt-doped samples was performed with LabRAM HR (Jobin Yvon Horiba). An argon laser with λ=488 nm (power 10 mW) and BX41 (Olympus) microscope and 100x objective lens with a spot size of less than 1 μm was used. The I(D)/I(G) ratio was found by fitting a double Gaussian fitting function. The I(D)/I(G) ratio is known to correlate with the sp^2/sp^3 fraction and the density of the film [24,30].

XPS was carried out with Kratos ULTRA electron spectrometer (Kratos Analytical, Manchester, UK) using monochromated Al Kα X-ray irradiation at 100 W. Samples were measured after overnight pre-evacuation using ash-free cellulose filter paper as *in-situ* reference material [31]. Fitting of the high resolution data was done assuming Gaussian lineshapes. The binding energies (BE) were calibrated by using C 1s at 285.0 eV as the reference [32]. Pt was fitted into two doublets by using predefined BE split and predefined Pt 4f 7/2:5/2 split ratios.

2.3 Electrochemical Measurements

Electrochemical experiments were performed with a Gamry Reference 600 potentiostat (Gamry Instruments), CHI 630E potentiostat (CH Instruments, Inc.) or a digital recorder (eDAQ ED401) and a potenciostat (Edaq EA161) coupled to a signal generator (PAR 175). In rotating disk electrode experiments with a Radiometer Analytical rotating motor (Model EDI101) was utilized. Reference electrode was a Ag/AgCl/KCl sat'd electrode (+0.199 vs. SHE, Radiometer Analytical) and counter electrode a carbon rod or a Pt wire.

In order to clean the samples, they were first subject to potential cycling in nitrogen purged and blanketed 0.15 M H_2SO_4 (diluted in deionized water with resistivity of 18.2 MOhm cm from Merck Millipore Emsure 95-97 % H_2SO_4) for at least 100 cycles between -0.2 V and 1.2 V vs. Ag/AgCl

with 1 V s^{-1}. Electrochemical characteristics were inspected by cyclic voltammetry in 1 mM FcMeOH (Sigma) dissolved in 0.15 M H_2SO_4.

Scan rates and peak currents for voltammetric data can be connected through Randles-Sevcik equation

$$I_p = (2.69 \times 10^5) n^{\frac{2}{3}} A D^{\frac{1}{2}} v^{\frac{1}{2}} C_0, \quad (1)$$

where I_p is the peak current, n is the number of transferred electrons (for FcMeOH n = 1), A is the effective surface area, D is the diffusion coefficient (2.17 x 10^{-5} cm^2 s^{-1} [33]) and C_0 is the bulk concentration of FcMeOH (1 mM). The effective surface area was approximated by the geometric area of the sample (0.031 cm^2 for a-C/Pt samples and 0.071 cm^2 for Pt samples). For evaluation of heterogeneous rate constants, k_e, from FcMeOH measurements, method presented by Nicholson [34] was used:

$$\psi = \gamma^{\alpha} k_e / \sqrt{\pi a D_0}, \quad (2)$$

where γ is the square root of the ratio for diffusion coefficients for oxidized and reduced forms of FcMeOH (here assumed to be unity), α is the charge transfer coefficient (approximated to be 0.5), $a = nFv/RT$ (F is Faraday's constant 96 485 C/mol, R is universal gas constant 8.314 J/kmol), and D_0 is the diffusion coefficient of ferrocene. ψ values as function of peak potential separation were taken from the paper by Nicholson [34]. As equation (1) is only valid for reversible systems, it should be noted that sufficiently high k_e values obtained from analysis based on equation (2) indicate that the system can be assumed to be reversible. For H_2O_2 experiments, a stock solution of 10 mM was freshly prepared from 30 % H_2O_2 (Merck KGaA, Germany) by dilution in deionized water. This stock solution was then pipetted into the cell filled with phosphate buffered saline (PBS, pH 7.4) containing NaCl (137 mM), KCl (2.7 mM), Na_2HPO_4 (10 mM) and KH_2PO_4 (1.8 mM). During the chronoamperometric measurements the sample was first held at 0.3 V vs. Ag/AgCl or 30 s before stepping the potential to -0.2 V vs. Ag/AgCl for H_2O_2 reduction.

For the CO adsorption experiments the 0.15 M H_2SO_4 (diluted from 96 % Merck suprapur H_2SO_4) was bubbled with CO (Air Liquide N46) for 5 minutes at open circuit until saturation. Next, the sample was immersed in the cell at -0.099 vs. Ag/AgCl for two minutes. After that, CO was removed from the cell by purging with Ar (Air Liquide 99.999 %) for 15 minutes. Finally, the voltammetric profile was registered. For consistency the graphs presented here have been plotted against Ag/AgCl even though the reference electrode in the CO stripping experiments was RHE (H_2 purity Air Liquide 99.999 %).

3. Results and Discussion

3.1.Structural Characterization

Transmission Electron Microscopy (TEM)

Figure 1 show the HRTEM micrographs of a-C/Pt film deposited on NaCl crystal. It can be seen that immediately after the deposition, the structure is very finely dispersed and relatively homogeneous (Figure 1A). There are only very small Pt precipitates or Pt-rich areas inside the amorphous carbon matrix. Further, it is likely that most of the Pt is still covered by a thin carbon over layer. When the surface is bombarded with electrons (i.e., held under the electron beam), Pt atoms gain sufficient energy to facilitate their surface diffusion and thus significant coarsening can be seen to occur, since, the initial finely dispersed structure is highly metastable and, if given the opportunity, will start to coarsen, driven by the minimization of the surface free energy of the system. In Figure 1B, clear Pt precipitates are already visible and they can be seen to gradually grow as the electron bombardment continues (Figures 1C and D). It is quite likely that similar coarsening occurs also during electrochemical oxidation and reduction cycles, though probably to a lesser degree (see below).

To our knowledge there exists only a few earlier studies on a-C films with Pt alloying, which can be used to benchmark the results from our films. For example, in study by Lamber & Jaeger [35] Pt-carbon multilayer films were prepared and these films were investigated with high resolution electron microscopy. Heating the samples caused sintering of Pt particles resembling the phenomena seen in Figure 1. However, in Lamber & Jaeger Pt was not alloyed with amorphous carbon but instead supported on it. Similarly, in Fabbri et al. [36] Pt was deposited on top of an amorphous carbon film TEM grids by sputtering to inspect the resulting particle size. With Pt-loading of 2 µg cm^{-2} they obtained both 2-3 nm diameter particles and larger agglomerates resembling our films after prolonged electron bombardment (Figure 1D). Increasing the deposition time and thus Pt-loading over 20 µg cm^{-2} caused further formation of Pt agglomerates and particulate layers. Fabbri et al. referred to a study by Schwanitz et al. [37] where it was stated that even with loadings less than 3 µg cm^{-2}, Pt nanoparticles and agglomerates coexist. Increasing the loading (i.e. deposition time) increases also agglomeration. Fabbri et al. did not, however, specify the time the samples were kept under electron bombardment which might also have had an effect on agglomeration. Further, the deposition of a-C and Pt occurs in our case by consecutive pulses thus being quite a different process than that used by both Lamber & Jaeger and Fabbri et al. Moreover, energy during the cathodic vacuum arc deposition is considerably larger compared to sputtering which explains the more refined structure of our films.

Raman Spectroscopy

The background subtracted Raman spectra of the ta-C and a-C/Pt samples are presented in Figure 2A. No smoothing of the data was performed. Figure 2A shows the actual measured background subtracted signal, the fitted D and G peaks as well as the cumulative fit. I(D)/I(G) ratios for ta-C and a-C/Pt are 0.56 and 0.66, respectively. The intensity of the Raman signal decreases while the I(D)/I(G) ratio increases with the addition of Pt. It has been shown by Ferrari and Robertson [38]

that sp^2 sites contribute more to visible Raman spectra compared to sp^3 sites. The G peak is mainly related to sp^2 vibrations whereas the source of D peak is aromatic rings. In most cases, it is not possible to define the sp^3 fraction from visible Raman spectrum. However, the I(D)/I(G) ratio can be related to sp^2/sp^3 content: increase in I(D)/I(G) ratio is likely caused by an increase in the sp^2 fraction in the Pt containing film [38]. The results shown here are also in agreement with preceding results obtained with similar films [28,39]. What has been stated above points out that the inclusion of Pt into the growing ta-C films reduces the amount of sp^3 and consequently changes the ta-C into an a-C film.

X-ray Photoelectron Spectroscopy (XPS)

XPS spectra (wide and high-resolution spectra for Pt 4f, N 1s, C 1s and O 1s) for Pt-doped a-C film are presented in Figure 2B. The spectra indicated the presence of carbon (77.4 at-%), oxygen (12.9 at-%), platinum (6.4 at-%) and nitrogen (1.9 at-%) in the films. In addition, we also observed traces of silicon (0.7 at-%) and titanium (0.5 at-%). The amounts of N, O, Ti and Si are comparable with our previous results obtained with pure ta-C [40]. The amount of C-C bonded carbon was over 80 %, while remaining carbon was most probably bound to surface oxygen species, typically found on all air-exposed surfaces.

After deposition of the a-C/Pt film, the wafers were cut with dicing saw which might have resulted in Si contamination of the surface. This is supported by the Si peak not showing any background [41]. On the other hand, the strong background after the tiny Ti signal clearly points toward the fact that Ti is buried under the a-C/Pt layer [41], thus originating from the Ti adhesion layer used between Si and a-C/Pt layer.

Strong backgrounds after XPS signals originating from platinum likewise promote the idea that Pt is present as nanoscale particles or islands, not as a monolayer. This argument is supported by the following facts:

(i) First, the shape of the pronounced background tailing for all Pt peaks indicates that the depth distribution of platinum atoms extend to some nanometers, so it is more than just a monolayer or two [41].

(ii) Secondly, the amount of Pt (6.4 at-%) is too low for a continuous thin layer of thickness indicated by the peak shape.

As for the valence state, the major contribution from platinum originates from metallic zero valent state. The main peaks are slightly shifted from reference values characteristic for metallic Pt 4f, which further supports that Pt is present as isolated particles on insulating sandwich structured substrate. Furthermore, there is a minor component at around 74 eV, suggesting presence of Pt oxide over layer [42], and this is further confirmed by MeO_x component broadening in the oxygen O 1s spectra.

Atomic-Force Microscopy (AFM)

AFM topography maps for fresh sample and samples cycled in 0.15 M H_2SO_4 at 1 V/s between -0.2 V and 1.4 V vs. Ag/AgCl are presented in Figure 3. They exhibit similar structural features to the HRTEM micrographs (Figure 1). However, the features in topography maps are an order of magnitude coarser. This is most likely due to the convolution effect of the AFM tip with the surface topography. Interestingly, when the sample was cycled between -0.2 V – 1.4 V vs. Ag/AgCl the surface became less smooth with larger differences in particle sizes. Surface roughness from AFM measurements values for samples with varying upper potential limit (E_{up}) are compared in Figure 3C. Interestingly, there is a sudden and significant increase in surface roughness when E_{up} = 1.4 V

which further supports the suggestion that the surface is coarsened with potential cycling after a certain threshold potential is reached.

It is evident from the above TEM, Raman, XPS and AFM results that the a-C films contain most likely carbon-covered oxidized Pt islands with a narrow size distribution. Based on the changes seen during TEM investigations the structure will coarsen by electron bombardment. It is proposed that this is likely to also occur to some degree during CV experiments, especially prolonged cycling in wide potential window as shown by the AFM results above. The latter coarsening arises from small Pt particles dissolving during the positive scan and their re-deposition on larger particles during the negative scan.

3.2. Electrochemical Characterization

Cyclic Voltammetry in Sulfuric Acid

Figure 4 shows the effect of prolonged cycling in 0.15 M H_2SO_4 at 1 V/s. Pt features (H_2 adsorption/desorption, Pt(OH) formation/reduction) become more evident as the cycling is proceeded. Moreover, Pt(OH) reduction peak is shifted anodically towards the "bulk" value (see Conway et al. [43] for details) which is suggested to be related to coarsening of the structure and formation of larger Pt island from small, separate particles. This is in line with results obtained by Solla-Gullón et al. [44] with carbon nanotube supported Pt nanoparticles. The results are also consistent with other previous studies where it has been shown that the Pt oxide reduction peak shifts to more positive voltages with increasing particle size [36,45–49]. This behavior has been explained by oxygen species (especially OH) adsorbing more strongly when Pt particle size is decreased [50,51]. In addition to the coarsening of the structure, the Pt surface is cleaned during the cycling. This is manifested by the decreasing oxidation current above 1 V and increasing current in the hydrogen region below 0.1 V. However, the current in the hydrogen region starts to decrease

after 100 cycles which is related to agglomeration of Pt and decreasing of electrochemically active Pt surface area [44]. This was further verified by calculating the active area from the charges in the hydrogen desorption region by integrating the area from the CV curve taking the current in the double-layer region as baseline and dividing this by charge density (210 μC/cm^2) for 100th and 200th cycles. The active Pt surface area was decreased from 6.70 x 10^{-3} cm^2 to 5.31 x 10^{-3} cm^2. It is assumed here that the active surface area calculated from the hydrogen desorption includes only the contribution from Pt and omits the possible activity of a-C. Thus, the geometric area of the sample was used for calculating current densities. Hence, it can be concluded that cycling the potential in H_2SO_4 resulted into both cleaning of the Pt islands from (mainly carbon) impurities and coarsening of the very finely dispersed initial structure.

Cyclic Voltammetry in 1 mM Ferrocenemethanol

Figure 5 shows the results for potential cycling in 1 mM ferrocenemethanol (FcMeOH) at different scan rates. The peak separations ΔE_p at different scan rates (Table 1) indicate reversible redox process. This is further supported by the j_{ox}/j_{red} ratio being close to unity and sufficiently large value of k_e = 0.45 cm s^{-1} calculated by using the Nicholson method [34] and averaged for different scan rates. Peak current densities calculated with geometric areas by using Randles-Sevcik equation for oxidation of FcMeOH on Pt are also included in **Error! Reference source not found.**. Values are relatively close in magnitude to those obtained with a-C/Pt even though there is no uniform Pt layer on a-C/Pt surface. Streeter et al. [52] studied voltammetry at nanoparticles and divided the diffusional behavior of samples with nanoparticles into four categories depending on the diffusion layer thickness with respect to the electrode size. Comparable peak current densities for a-C/Pt and Pt samples indicate that our samples would fall into category 4 where overlapping diffusion zones

result in planar diffusion field. On the other hand, Streeter et al. also stated that negative deviation from Randles-Sevcik curve (supporting information Figure S1) indicates incompletely overlapping diffusion zones which would place our a-C/Pt samples into category 3. However, regardless of the exact category it is most likely that Pt particles or island in a-C/Pt do not behave as isolated particles, but form a mutual planar diffusion zone and the thickness of the diffusion layer is large with respect to the particle radius.

Rotating Disk Electrode Measurements

Results from rotating disk electrode (RDE) experiments in 0.15 M H_2SO_4 containing 1 mM H_2O_2 for Pt and a-C/Pt samples are presented in Figure 6 and Figure 7, respectively. For both sample types, the cathodic and anodic scans started from upper (1 V vs. Ag/AgCl) and lower (-0.2 V vs. Ag/AgCl) potential limits, respectively. Pt sample shows expected behavior with distinct plateaus for both H_2O_2 oxidation and reduction at 50 mV/s. However, a-C/Pt results are less straightforward. The current is dependent on the rotation rate in the anodic end, but only marginally at the cathodic end

It has been shown that H_2O_2 reacts with Pt surface chemically and the detected current arises from the regeneration of suitable Pt sites [23]:

At the cathodic end

$2Pt + H_2O_2 \rightarrow 2Pt(OH)$ (dissociative adsorption of H_2O_2) (3)

$2\,Pt(OH) + 2H^+ + 2e^- \rightarrow 2\,Pt(H_2O)$ (regeneration of oxide-free Pt sites) (4)

At the anodic end

$2Pt(OH) + H_2O_2 \rightarrow 2Pt(H_2O) + O_2$ (non-electrochemical oxidation of H_2O_2) (5)

$2Pt(H_2O) \rightarrow 2Pt(OH) + 2H^+ + 2e^-$ (regeneration of oxidized Pt sites) (6)

Moreover, as OH species are more strongly adsorbed to small particles compared to bulk Pt [50,51] we propose that the behavior observed for a-C/Pt during RDE experiments arises from OH desorption induced complications. In fact, as Han et al. have shown [51] by utilizing detailed DFT calculations OH adsorption on nanosized Pt particles is not only significantly stronger than on extended (bulk) Pt surfaces, but also the preferential sites for OH adsorption were different on small particles and in the bulk samples. What we propose is the following:

(i) At the cathodic end, to generate the current, combining of surface bound OH particles is required [equation (4)]. This is possibly partly hindered by the large adsorption strength of OH to the Pt nanoparticles.

(ii) During the cathodic scan the reduction of OH sites is only partial due to their large adsorption strength. It is also possible that the reduction of Pt oxide is gradual and depends on the specific particle size leading to the observed tilted current curve. As a consequence, the kinetics appears to be slower for the cathodic scan.

(iii) At the anodic end, strong OH adsorption favors the electrochemical step [equation (6)] resulting in high currents. However, based on the shape of the current curve the reaction is not entirely governed by mass transport here either. From Levich equation [equation (S1)] and using the effective area calculated from the currents of Figure 5 using Randles-Sevcik equation [equation (1)], diffusion limited current (see Supporting Information) of ca. 430 and 1075 μA cm^{-2} are predicted for 400 and 2500 rpm, respectively, which supports the idea that experimental currents are slightly lower than the diffusion limited current, especially for the higher rotation rate.

(iv) H_2O_2 reactions on Pt require suitable active sites to proceed as shown in eqs. (3)-(6). It is thus possible that owing to the small amount and size of the Pt islands the number of available reaction sites start to limit the extent of reaction on Pt despite the enhanced mass transport resulting from the increased rotating speed.

In addition, the zero current crossing point is shifted to cathodic direction for the cathodic scan reflecting the strong OH adsorption (see the dashed lines in Figure 7).

In order to obtain more information on the suggested partial reduction of OH sites during the cathodic scan (item (ii) in the previous list) we compared the effect of upper potential limit on the current in the cathodic end of the voltammograms. The sample potential was first cycled at 1 V/s in 0.15 M H_2SO_4 between -0.2 V and 1.2 V (vs. Ag/AgCl) in order to clean the surface. Next, the sample potential was cycled in the same solution between -0.2 V and 0.4 V at 50 mV/s. As the upper potential limit is sufficiently low, there is no OH adsorption in this case. As shown in Figure 8A, when cycling to upper potential limit of 1.2 V is carried out there is clear increase in the magnitude of the current during the cathodic scan in the hydrogen adsorption region in comparison to cycling only up to 0.4 V. As the anodic current for hydrogen desorption match for both upper potential limits there has to be other source than hydrogen adsorption for the increase in current. This additional current is proposed to originate from desorption of OH indicating that it indeed remains adsorbed down to the low potential limit. For polycrystalline Pt (Figure 8B) there is no such increase in the current magnitude with increased upper potential limit which demonstrates that the strong OH adsorption is related to small islands and not to bulk Pt.

CO Stripping Experiments

To have more insight into the role of the size of the Pt particles, two cleaning protocols with different upper potential limits were carried out in H_2SO_4 (Figure 9A). The hypothesis behind this was that the more extensive cleaning with the wider potential window should result in a larger average particle size. This is supported by AFM results in Figure 3 where it is shown that increasing the upper potential limit indeed leads to coarser structure. The sample cleaned with the lower upper potential limit still shows hydrogen adsorption peaks but in significant less extent than the sample with more extensive cleaning. This indicates that platinum particles in this sample are still partially covered by carbon that has not been removed in the cleaning process.

After cleaning as indicated above samples were used in CO-stripping experiments. CO was first adsorbed on the sample surface by CO bubbling in the working solution during 2 minutes at a controlled potential of -0.099 vs. Ag/AgCl. After purging the excess CO out from the cell with Ar, remaining CO adsorbed on the platinum surface was electrochemically oxidized by scanning the potential to sufficiently positive values. As seen in Figure 9B there is a significant anodic shift of the CO oxidation peak when the Pt particles are smaller, i.e. the upper potential limit was lower during the cleaning protocol.

To rationalize the observed behavior, let us consider the corresponding reactions during CO-oxidation, which are typically given as:

$$H_2O + * \leftrightarrow OH_{ads} + H^+ + e^- \quad (7)$$

$$CO_{ads} + OH_{ads} \rightarrow COOH_{ads} \quad (8)$$

$$COOH_{ads} \rightarrow CO_2 + H^+ + e^- + * \quad (9)$$

where * indicates a free surface site.

There have been a lot of investigations about the effect of Pt particle size on the CO-oxidation currents. Kabbabi et al.[45] suggested that decreasing Pt particle size correlates with both strong

adsorption of oxygenated species as well the anodic shift for the CO oxidation. In Maillard et al. [53] the authors stated that CO oxidation peak moved to more anodic potentials as the Pt-particle size decreased. This was attributed to strong OH adsorption on nanoparticles (NPs) and partly also to strong interaction of CO with the NPs that slows down its surface diffusion. They also observed a peak in the double layer region of CO-free CVs in H_2SO_4 which they attributed to (bi)sulfate adsorption on Pt. In another study Maillard et al. showed consistent results with the previous one, except that they attributed the peak in CO-free H_2SO_4 CV observed earlier to quinone couple on oxidized glassy carbon support [54]. Further, in a third study by Maillard et al. the conclusions about the size effects of Pt-particles were again the same as in the two earlier papers [55]. However, in this case the authors emphasized more the role of hindered CO diffusion on Pt nanoparticles, but still recognized the effect of strong adsorption of OH.

In publication by Arenz et al. similar shift towards higher anodic potentials as a function of decreasing particle radius was shown to take place, but in this case the authors attributed the effect mainly to the ability of different sizes of nanoparticles to form OH_{ads} on defect sites rather than to the CO energetics [56]. Mayrhofer et al. have shown, by utilizing the method described by Climent et al. [57], that the potential of total zero charge shifted approximately 35 mV negative by decreasing the particle size from 30 nm down to 1 nm [49]. They also stated that OH adsorption was similarly enhanced to small particles consistent with the other investigations.

Mayrhofer et al. showed that there was a shift in the CO-oxidation potential as a function of particle size, but the onset potential really changed to less anodic values only when one moved from 5 nm sized to 30 nm sized particles [58]. Contrary to the results shown by Maillard et al. [53–55], they showed that within the particle size range of 1-5 nm the onset potential was more or less constant. The shift was mainly attributed to stronger CO adsorption and thus lower CO surface mobility on small Pt nanoparticles.

There is also evidence that CO forms a more compact adsorption layer on top of Pt nanoparticles than on extended surfaces [55]. Based on the equations (7)-(9) water has to be able to penetrate between the adsorbed CO molecules to form the required OH adsorption sites on Pt surface. It is thus possible that H_2O cannot easily penetrate between the more compact layer of adsorbed CO on smaller Pt-particles, which would then hinder the onset of the CO-oxidation reaction. This is in line with the conclusions made by Arenz et al. [56] i.e. that the CO oxidation reaction is mainly influenced by the ability of Pt nanoparticles with different sizes to form OH_{ads}, which would be in fact controlled by the compactness of adsorption layer formed by CO that in turn depends on particle size.

Whatever is the exact mechanism that controls the CO oxidation reaction it is evidently dependent on the particle size used in this study, which based on the AFM and TEM characterization changes from a few nanometers (as deposited samples) to the range of 30-50 nm (extensively cleaned samples). Thus, the range of particle sizes where the effects can be seen in this study are consistent with the statements made by Mayrhofer et al. [58]. Also from XPS results it was evident that as deposited samples surfaces contained Pt islands that were partly covered with thin oxide layer. As it has been shown, both experimentally and by simulations, that the adsorption of OH is also strongly dependent on the particle size, it is plausible that the differences in particle sizes and distribution leads to the behavior observed both in RDE experiments with H_2O_2 and CO stripping. It must, however, be noted that the root causes behind these observations are not unambiguously known at the moment and further investigations are needed.

Chronoamperometry

Despite the complications in understanding the fundamental electrochemical behavior of a-C/Pt samples they were successfully used to detect H_2O_2 in PBS (pH 7.4) with amperometry (-0.2 V vs.

Ag/AgCl). They showed linearity between 50 µM and 1000 µM (R^2 = 0.999) with sensitivity of 0.32 µA $µM^{-1}$ cm^{-2} (Figure 10) and limit of detection of 0.32 µM (S/N = 3). The H_2O_2 response deviates from that obtained in blank PBS already before 0.05 s from the start of the measurement (inset in Figure 10). Even though H_2O_2 oxidation on a-C/Pt would be kinetically less limited compared to the reduction at large negative overpotentials, it would also result in oxidation of interfering species in biosensing applications. For example dopamine and ascorbic acid are expected to react at similar overpotentials on a-C/Pt as they do on ta-C films [59].

Even though the linear range obtained for a-C/Pt samples does not extend down to the nanomolar range that would be needed for example for the (enzymatic) detection of neurotransmitter glutamate, the hybrid material presented here shows great promise as an electrochemical sensor for H_2O_2 detection. One of the main advantages is that compared to, for example, various carbon nanonmaterials based applications a-C/Pt is compatible with micro- and nanofabrication methods as is, which makes it suitable for manufacturing of devices.

4. Conclusions

Structural and electrochemical characterization of a-C thin films containing intrinsic Pt-gradient was presented in this work. It was shown that continuous electron bombardment in TEM resulted in coarsening of the initially finely dispersed structure and formation of Pt islands. Similar structural changes occurred during cycling in H_2SO_4 based on the AFM measurements and CO stripping experiments. Rotating disk electrode measurements carried in 0.15 M H_2SO_4 with 1 mM H_2O_2 indicated that OH adsorption/desorption may partly control both oxidation and reduction of H_2O_2 on a-C/Pt films. This is likely to be caused by stronger adsorption of OH on small Pt islands compared to bulk Pt. Finally, it was shown that, despite the complications in the exact reaction mechanisms, a-C/Pt films showed extended linear response for H_2O_2 reduction in neutral solution (PBS). Thus, these CMOS compatible thin films provide an interesting and promising platform for

hydrogen peroxide detection, although further investigations are needed to clarify the details of the chemical and electrochemical reactions on the surfaces of these films.

Acknowledgements

Academy of Finland (E.P. grant #274670, T.L. grants # 285015 and #285526), Biocentrum Helsinki, Finnish Cultural Foundation (N.I. grant #00160331) and Foundation for Aalto University Science and Technology are acknowledged for funding. Yanling Ge is acknowledged for operating the TEM. The authors also acknowledge the provision of facilities at Micronova Nanofabrication Center.

5. References

[1] A.J. Bard, L.R. Faulkner, Electochemical methods: Fundamentals and Applications, 2nd ed., Wiley and Sons, Hoboken, NJ USA, 2001.

[2] A.M. Gómez-Marín, K.J.P. Schouten, M.T.M. Koper, J.M. Feliu, Interaction of hydrogen peroxide with a Pt(111) electrode, Electrochem. Commun. 22 (2012) 153–156. doi:10.1016/j.elecom.2012.06.016.

[3] A. Schneider, L. Colmenares, Y.E. Seidel, Z. Jusys, B. Wickman, B. Kasemo, R.J. Behm, Transport effects in the oxygen reduction reaction on nanostructured, planar glassy carbon supported Pt/GC model electrodes., Phys. Chem. Chem. Phys. 10 (2008) 1931–43. doi:10.1039/b719775f.

[4] H.S. Wroblowa, Yen-Chi-Pan, G. Razumney, Electroreduction of oxygen a new mechanistic criterion, J. Electroanal. Chem. 69 (1976) 195–201.

[5] M. Giorgio, M. Trinei, E. Migliaccio, P.G. Pelicci, Hydrogen peroxide: a metabolic by-product or a common mediator of ageing signals?, Nat. Rev. Mol. Cell Biol. 8 (2007) 722–8. doi:10.1038/nrm2240.

[6] T.P. Szatrowski, C.F. Nathan, Production of large amounts of hydrogen peroxide by human tumor cells, Cancer Res. 51 (1991) 794–798.

[7] B.T. Chen, M. V Avshalumov, M.E. Rice, T. Billy, M. V Avshalumov, M.E. Rice, H_2O_2 is a novel, endogenous modulator of synaptic dopamine release, J. Neurophysiol. 85 (2001) 2468–2476.

[8] Q.H. Gibson, B.E.P. Swoboda, V. Massey, Kinetics and mechanism of action of glucose oxidase, J. Biol. Chem. 239 (1964) 3927–3934.

[9] H. Kusakabe, Y. Midorikawa, T. Fujishima, A. Kuninaka, H. Yoshino, Purification and properties of a new enzyme, L-glutamate oxidase, from Streptomyces sp. X-119-6 grown on wheat bran., Agric. Biol. Chem. 47 (1983) 1323–1328. doi:10.1271/bbb1961.47.1323.

[10] Q.K. Yue, I.J. Kass, N.S. Sampson, A. Vrielink, Crystal structure determination of cholesterol oxidase from streptomyces and structural characterization of key active site mutants, Biochemistry. 38 (1999) 4277–4286. doi:10.1021/bi982497j.

[11] E. Aschauer, R. Fasching, G. Urban, G. Nicolussi, W. Husinsky, Surface characterization of thin-film platinum electrodes for biosensors by means of cyclic voltammetry and laser SNMS, J. Electroanal. Chem. 381 (1995) 143–150. doi:10.1016/0022-0728(94)03656-N.

[12] S.A.G. Evans, J.M. Elliott, L.M. Andrews, P.N. Bartlett, P.J. Doyle, G. Denuault, Detection of Hydrogen Peroxide at Mesoporous Platinum Microelectrodes, Anal. Chem. 74 (2002) 1322–1326. doi:10.1021/ac011052p.

[13] R. Zeis, T. Lei, K. Sieradzki, J. Snyder, J. Erlebacher, Catalytic reduction of oxygen and hydrogen peroxide by nanoporous gold, J. Catal. 253 (2008) 132–138. doi:10.1016/j.jcat.2007.10.017.

[14] F. Meng, X. Yan, J. Liu, J. Gu, Z. Zou, Nanoporous gold as non-enzymatic sensor for hydrogen peroxide, Electrochim. Acta. 56 (2011) 4657–4662. doi:10.1016/j.electacta.2011.02.105.

[15] J.S. Jirkovský, M. Halasa, D.J. Schiffrin, Kinetics of electrocatalytic reduction of oxygen and hydrogen peroxide on dispersed gold nanoparticles, Phys. Chem. Chem. Phys. 12 (2010) 8042–8052. doi:10.1039/c002416c.

[16] C.M. Welch, C.E. Banks, a O. Simm, R.G. Compton, Silver nanoparticle assemblies supported on glassy-carbon electrodes for the electro-analytical detection of hydrogen peroxide, Anal. Bioanal. Chem. 382 (2005) 12–21. doi:10.1007/s00216-005-3205-5.

[17] G. Flätgen, S. Wasle, M. Lübke, C. Eickes, G. Radhakrishnan, K. Doblhofer, G. Ertl, Autocatalytic mechanism of H_2O_2 reduction on Ag electrodes in acidic electrolyte: experiments and simulations, Electrochim. Acta. 44 (1999) 4499–4506. doi:10.1016/S0013-4686(99)00184-X.

[18] S.B. Hall, E.A. Khudaish, A.L. Hart, Electrochemical oxidation of hydrogen peroxide at platinum electrodes. Part 1. An adsorption-controlled mechanism, Electrochim. Acta. 43 (1998) 579–588.

[19] S.B. Hall, E.A. Khudaish, A.L. Hart, Electrochemical oxidation of hydrogen peroxide at platinum electrodes. Part II: effect of potential, Electrochim. Acta. 43 (1998) 2015–2024. doi:10.1016/S0013-4686(97)10116-5.

[20] S.B. Hall, E.A. Khudaish, A.L. Hart, Electrochemical oxidation of hydrogen peroxide at platinum electrodes. Part III : Effect of temperature, Electrochim. Acta. 44 (1999) 2455–2462.

[21] S.B. Hall, E.A. Khudaish, A.L. Hart, Electrochemical oxidation of hydrogen peroxide at platinum electrodes. Part IV : phosphate buffer dependence, Electrochim. Acta. 44 (1999) 4573–4582.

[22] S.B. Hall, E.A. Khudaish, A.L. Hart, Electrochemical oxidation of hydrogen peroxide at platinum electrodes. Part V: inhibition by chloride, Electrochim. Acta. 45 (2000) 3573–3579. doi:10.1016/S0013-4686(00)00481-3.

[23] I. Katsounaros, W.B. Schneider, J.C. Meier, U. Benedikt, P.U. Biedermann, A.A. Auer, K.J.J. Mayrhofer, Hydrogen peroxide electrochemistry on platinum: towards understanding the oxygen reduction reaction mechanism, Phys. Chem. Chem. Phys. 14 (2012) 7384–7391. doi:10.1039/c2cp40616k.

[24] J. Robertson, Diamond-like amorphous carbon, Mater. Sci. Eng. R Reports. 37 (2002) 129–281. doi:10.1016/S0927-796X(02)00005-0.

[25] D.R. McKenzie, Tetrahedral bonding in amorphous carbon, Reports Prog. Phys. 59 (1996) 1611–1664.

[26] V. Protopopova, A. Iyer, N. Wester, A. Kondrateva, S. Sainio, T. Palomäki, T. Laurila, M. Mishin, J. Koskinen, Ultrathin undoped tetrahedral amorphous carbon films: The role of the underlying titanium layer on the electronic structure, Diam. Relat. Mater. 57 (2015) 43–52. doi:10.1016/j.diamond.2015.06.009.

[27] E. Kaivosoja, S. Sainio, J. Lyytinen, T. Palomäki, T. Laurila, S.I. Kim, J.G. Han, J. Koskinen, Carbon thin films as electrode material in neural sensing, Surf. Coatings Technol. 259 (2014) 33–38. doi:10.1016/j.surfcoat.2014.07.056.

[28] N. Tujunen, E. Kaivosoja, V. Protopopova, J.J. Valle-Delgado, M. Österberg, J. Koskinen, T. Laurila, Electrochemical detection of hydrogen peroxide on platinum-containing tetrahedral

amorphous carbon sensors and evaluation of their biofouling properties, Mater. Sci. Eng. C. 55 (2015) 70–78. doi:10.1016/j.msec.2015.05.060.

[29] E. Kaivosoja, N. Tujunen, V. Jokinen, V. Protopopova, S. Heinilehto, J. Koskinen, T. Laurila, Glutamate detection by amino functionalized tetrahedral amorphous carbon surfaces, Talanta. 141 (2015) 175–181. doi:10.1016/j.talanta.2015.04.007.

[30] R. McCann, S.S. Roy, P. Papakonstantinou, G. Abbas, J.A. McLaughlin, The effect of thickness and arc current on the structural properties of FCVA synthesised ta-C and ta-C:N films, Diam. Relat. Mater. 14 (2005) 983–988. doi:10.1016/j.diamond.2004.12.037.

[31] L.-S. Johansson, J.M. Campbell, Reproducible XPS on biopolymers: cellulose studies, Surf. Interface Anal. 36 (2004) 1018–1022. doi:10.1002/sia.1827.

[32] G. Beamson, D. Briggs, High resolution XPS of organic polymers, Wiley, 1992.

[33] J.E. Baur, R.M. Wightman, Diffusion coefficients determined with microelectrodes, J. Electroanal. Chem. Interfacial Electrochem. 305 (1991) 73–81. doi:10.1016/0022-0728(91)85203-2.

[34] R.S. Nicholson, Theory and application of cyclic voltammetry for measurement of electrode reaction kinetics, Anal. Chem. 37 (1965) 1351–1355. doi:10.1021/ac60230a016.

[35] R. Lamber, N.I. Jaeger, Electron microscopy study of the interaction of Ni, Pd and Pt with carbon, Surf. Sci. 289 (1993) 247–254. doi:10.1016/0039-6028(93)90657-6.

[36] E. Fabbri, S. Taylor, A. Rabis, P. Levecque, O. Conrad, R. Kötz, T.J. Schmidt, The Effect of platinum nanoparticle distribution on oxygen electroreduction activity and selectivity, ChemCatChem. 6 (2014) 1410–1418. doi:10.1002/cctc.201300987.

[37] B. Schwanitz, H. Schulenburg, M. Horisberger, A. Wokaun, G.G. Scherer, Stability of ultra-low Pt anodes for polymer electrolyte fuel cells prepared by magnetron sputtering, Electrocatalysis. 2 (2011) 35–41. doi:DOI 10.1007/s12678-010-0032-z.

[38] A.C. Ferrari, J. Robertson, Interpretation of Raman spectra of disordered and amorphous carbon, Phys. Rev. B. 61 (2000) 14095–14107. doi:10.1103/PhysRevB.61.14095.

[39] N. Menegazzo, C. Jin, R.J. Narayan, B. Mizaikoff, Compositional and electrochemical characterization of noble metal−diamondlike carbon nanocomposite thin films, Langmuir. 23 (2007) 6812–6818. doi:10.1021/la062582p.

[40] T. Palomäki, S. Chumillas, S. Sainio, V. Protopopova, M. Kauppila, J. Koskinen, V. Climent, J.M. Feliu, T. Laurila, Electrochemical reactions of catechol, methylcatechol and dopamine at tetrahedral amorphous carbon (ta-C) thin film electrodes, Diam. Relat. Mater. 59 (2015) 30–39. doi:10.1016/j.diamond.2015.09.003.

[41] S. Tougaard, Accuracy of the non-destructive surface nanostructure quantification technique based on analysis of the XPS or AES peak shape, Surf. Interface Anal. 26 (1998) 249–269. doi:10.1002/(SICI)1096-9918(199804)26:4<249::AID-SIA368>3.0.CO;2-A.

[42] J.F. Moulder, W.F. Stickle, P.E. Sobol, K.D. Bomben, Handbook of X-ray photoelectron spectroscopy: A reference book of standard spectra for identification and interpretation of XPS data, Perkin-Elmer, Physical Electronics Division, 1992.

[43] B.E. Conway, H. Angerstein-Kozlowska, W.B.A. Sharp, E.E. Criddle, Ultrapurification of water for electrochemical and surface chemical work by catalytic pyrodistillation, Anal. Chem. 45 (1973) 1331–1336. doi:10.1021/ac60330a025.

[44] J. Solla-Gullón, E. Lafuente, A. Aldaz, M.T. Martínez, J.M. Feliu, Electrochemical characterization and reactivity of Pt nanoparticles supported on single-walled carbon nanotubes, Electrochim. Acta. 52 (2007) 5582–5590. doi:10.1016/j.electacta.2006.11.051.

[45] A. Kabbabi, F. Gloaguen, F. Andolfatto, R. Durand, Particle size effect for oxygen reduction and methanol oxidation on Pt/C inside a proton exchange membrane, J. Electroanal. Chem. 373 (1994) 251–254. doi:10.1016/0022-0728(94)03503-2.

[46] Y. Takasu, N. Ohashi, X.G. Zhang, Y. Murakami, H. Minagawa, S. Sato, K. Yahikozawa, Size effects of platinum particles on the electroreduction of oxygen, Electrochim. Acta. 41 (1996) 2595–2600. doi:10.1016/0013-4686(96)00081-3.

[47] A. Gamez, D. Richard, P. Gallezot, F. Gloaguen, R. Faure, R. Durand, Oxygen reduction on well-defined platinum nanoparticles inside recast ionomer, Electrochim. Acta. 41 (1996) 307–314. doi:10.1016/0013-4686(95)00305-X.

[48] O. Cherstiouk, P. Simonov, E. Savinova, Model approach to evaluate particle size effects in electrocatalysis: preparation and properties of Pt nanoparticles supported on GC and HOPG, Electrochim. Acta. 48 (2003) 3851–3860. doi:10.1016/S0013-4686(03)00519-X.

[49] K.J.J. Mayrhofer, B.B. Blizanac, M. Arenz, V.R. Stamenkovic, P.N. Ross, N.M. Markovic, The impact of geometric and surface electronic properties of Pt-catalysts on the particle size effect in electrocatalysis, J. Phys. Chem. B. 109 (2005) 14433–14440. doi:10.1021/jp051735z.

[50] J. Tae Hwang, J. Shik Chung, The morphological and surface properties and their relationship with oxygen reduction activity for platinum-iron electrocatalysts, Electrochim. Acta. 38 (1993) 2715–2723. doi:10.1016/0013-4686(93)85090-L.

[51] B.C. Han, C.R. Miranda, G. Ceder, Effect of particle size and surface structure on adsorption of O and OH on platinum nanoparticles: A first-principles study, Phys. Rev. B. 77 (2008). doi:10.1103/PhysRevB.77.075410.

[52] I. Streeter, R. Baron, R.G. Compton, Voltammetry at nanoparticle and microparticle modified electrodes: theory and experiment, J. Phys. Chem. C. 111 (2007) 17008–17014. doi:10.1021/jp076923z.

[53] F. Maillard, E.R. Savinova, P.A. Simonov, V.I. Zaikovskii, U. Stimming, Infrared spectroscopic study of CO adsorption and electro-oxidation on carbon-supported Pt nanoparticles: interparticle versus intraparticle heterogeneity, J. Phys. Chem. B. 108 (2004) 17893–17904. doi:10.1021/jp0479163.

[54] F. Maillard, S. Schreier, M. Hanzlik, E.R. Savinova, S. Weinkauf, U. Stimming, R. Federation, Influence of particle agglomeration on the catalytic activity of carbon-supported Pt nanoparticles in CO monolayer oxidation, Phys. Chem. Chem. Phys. 7 (2005) 385–393.

[55] F. Maillard, M. Eikerling, O. V. Cherstiouk, S. Schreier, E. Savinova, U. Stimming, Size effects on reactivity of Pt nanoparticles in CO monolayer oxidation : The role of surface mobility, Faraday Discuss. 125 (2004) 357–377. doi:10.1039/b303911k.

[56] M. Arenz, K.J.J. Mayrhofer, V. Stamenkovic, B.B. Blizanac, T. Tomoyuki, P.N. Ross, N.M. Markovic, The Effect of the particle size on the kinetics of CO electrooxidation on high surface area Pt catalysts, J. Am. Chem. Soc. 127 (2005) 6819–6829. doi:10.1021/ja043602h.

[57] V. Climent, R. Gómez, J.M. Orts, A. Rodes, A. Aldaz, J.M. Feliu, Electrochemistry, spectroscopy, and scanning tunneling microscopy images of small single-crystal electrodes, in: Andrzej Wieckowski (Ed.), Interfacial Electrochem. Theory Exp. Appl., CRC Press, New York, 1999: pp. 463–475.

[58] K.J.J. Mayrhofer, M. Arenz, B.B. Blizanac, V. Stamenkovic, P.N. Ross, N.M. Markovic, CO surface electrochemistry on Pt-nanoparticles : A selective review, Electrochim. Acta. 50 (2005) 5144–5154. doi:10.1016/j.electacta.2005.02.070.

[59] S. Sainio, T. Palomäki, S. Rhode, M. Kauppila, O. Pitkänen, T. Selkälä, G. Toth, M. Moram, K. Kordas, J. Koskinen, T. Laurila, Carbon nanotube (CNT) forest grown on diamond-like carbon (DLC) thin films significantly improves electrochemical sensitivity and selectivity towards dopamine, Sens. Actuators, B. 211 (2015) 177–186. doi:10.1016/j.snb.2015.01.059.

Figure captions

Figure 1. HRTEM micrographs of a-C/Pt film grown on NaCl single crystals without Ti adhesion layer. The effect of prolonged electron bombardment from A to D is pronounced as the structure is coarsened. If A is taken as t = 0 s, the respective time points are B)

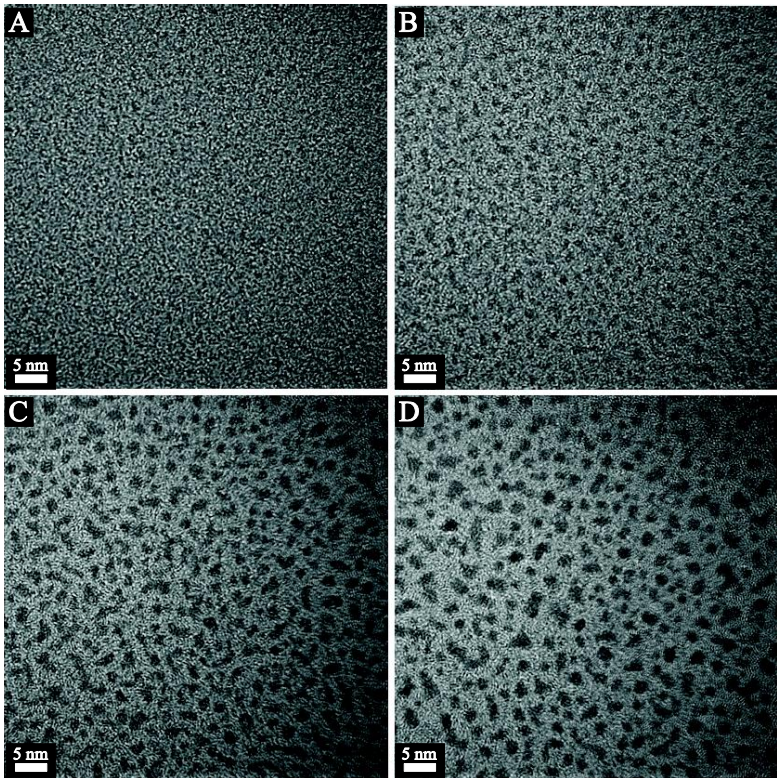

Figure 2. A) Raman spectra of ta-C and a-C/Pt samples. Increasing I(D)/I(G) ratio for a-C/Pt is likely caused by an increase in the sp^2 fraction. B) XPS wide area (large on the left) and high-resolution (four small on the right) spectra for a-C/Pt sample.

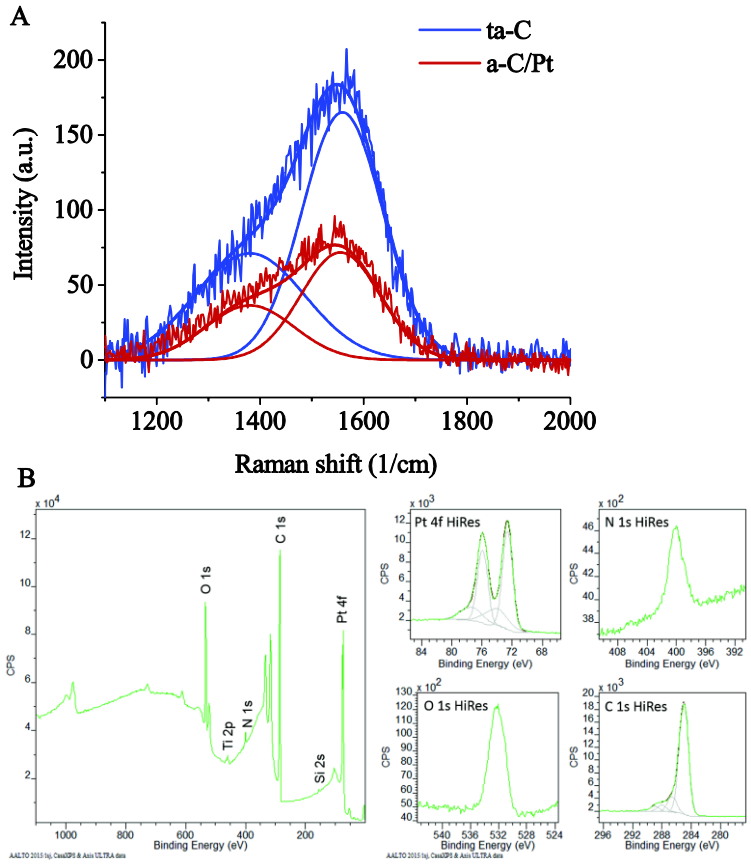

Figure 3. AFM topography maps for a-C/Pt samples. A) fresh sample and B) sample after prolonged cycling between -0.2 V and 1.4 V in 0.15 M H_2SO_4. Structural features are similar to those seen in HRTEM, though an order of magnitude coarser. C) Average surface roughness from AFM measurements for fresh sample samples cycled in 0.15 M H_2SO_4 with different upper potential limits. Standard deviations were used as error (N = 3).

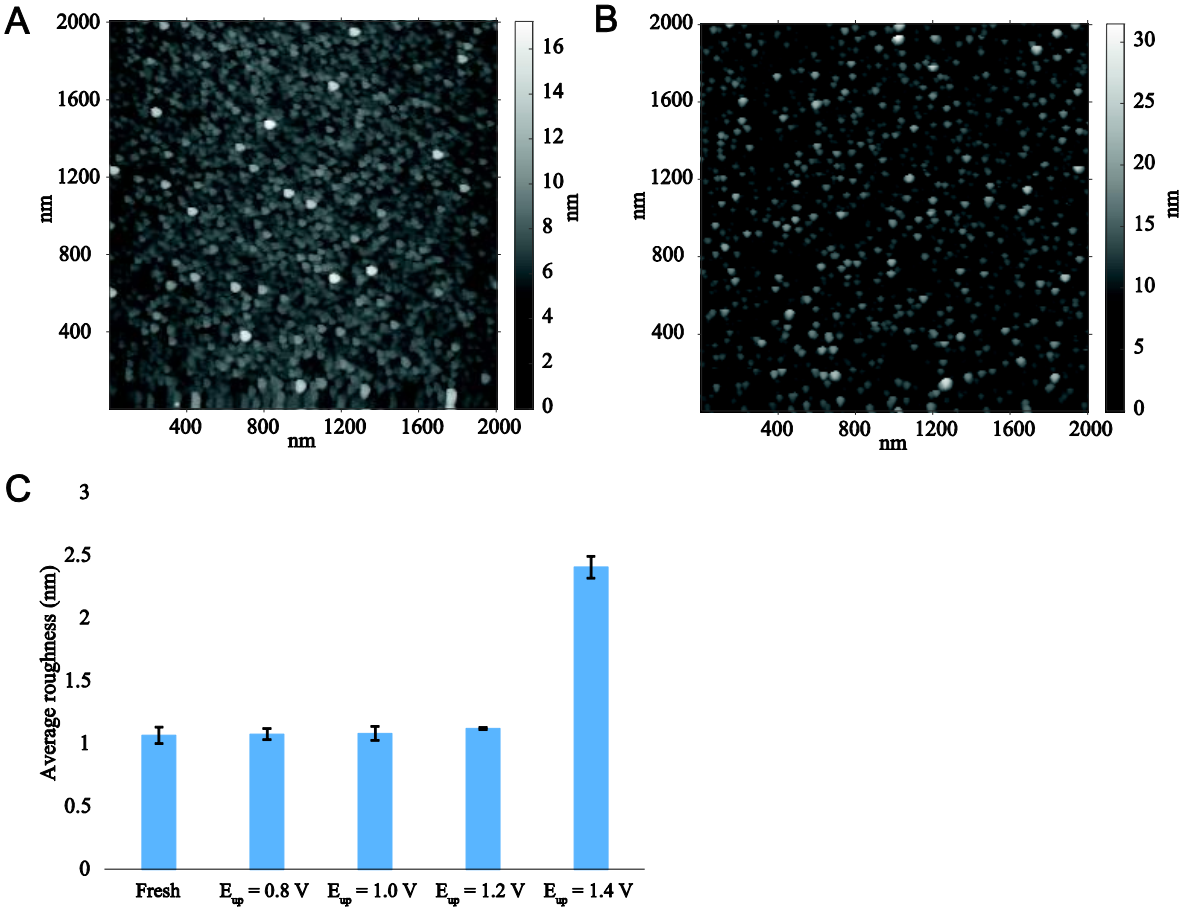

Figure 4. Cleaning cycling of a-C/Pt sample in 0.15 M H_2SO_4. Evolution of voltammograms during cleaning of a-C/Pt sample in 0.15 M H_2SO_4. Pt features become gradually more evident during prolonged cycling.

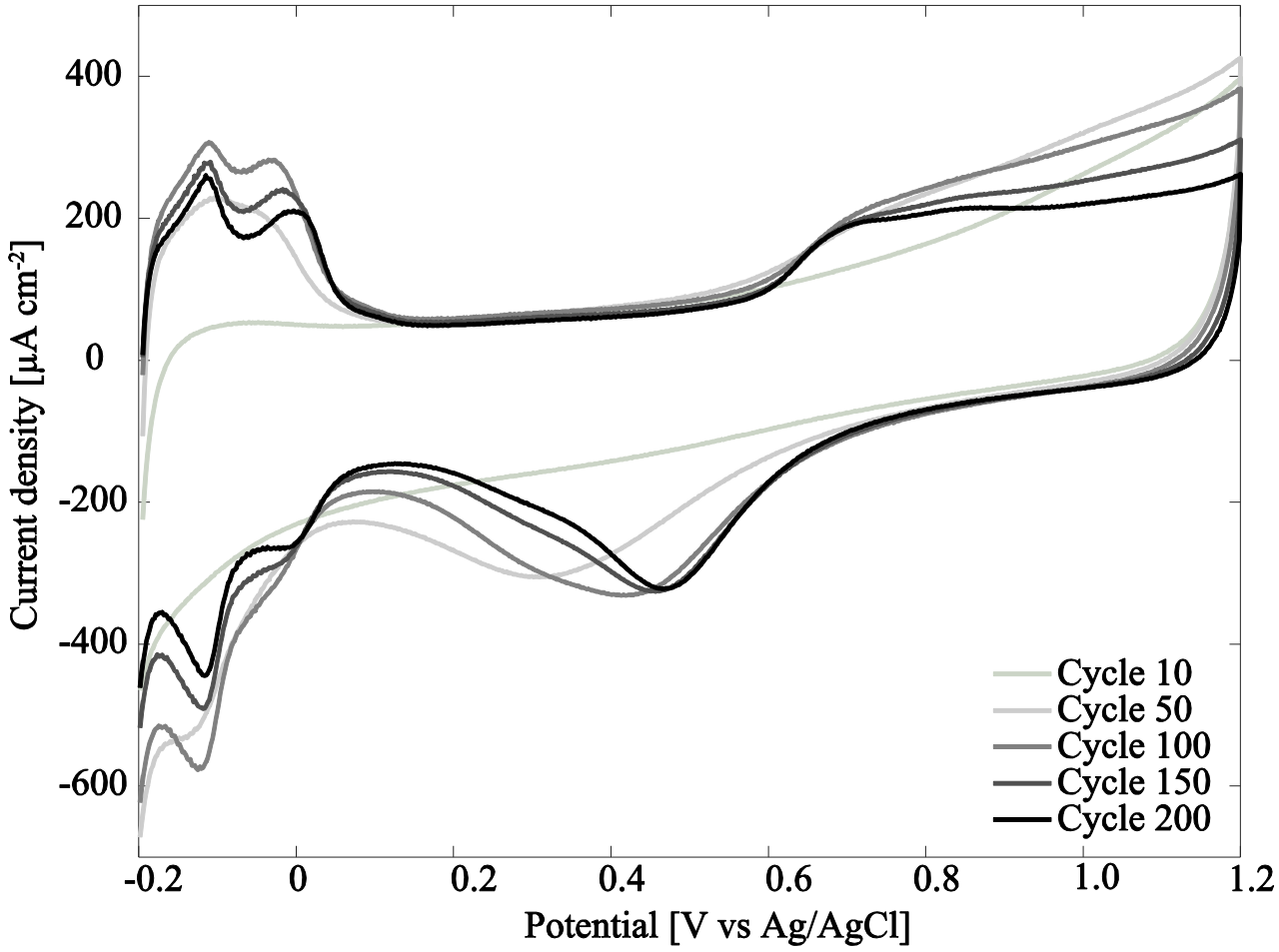

Figure 5. Cyclic voltammograms of a-C/Pt sample in 1 mM FcMeOH (dissolved in 0.15 M H_2SO_4) at different cycling rates. Sample shows nearly reversible behavior with ΔE_p being independent of scan rate and j_{ox}/j_{red} ratios close to unity for all except for 10 mV/s.

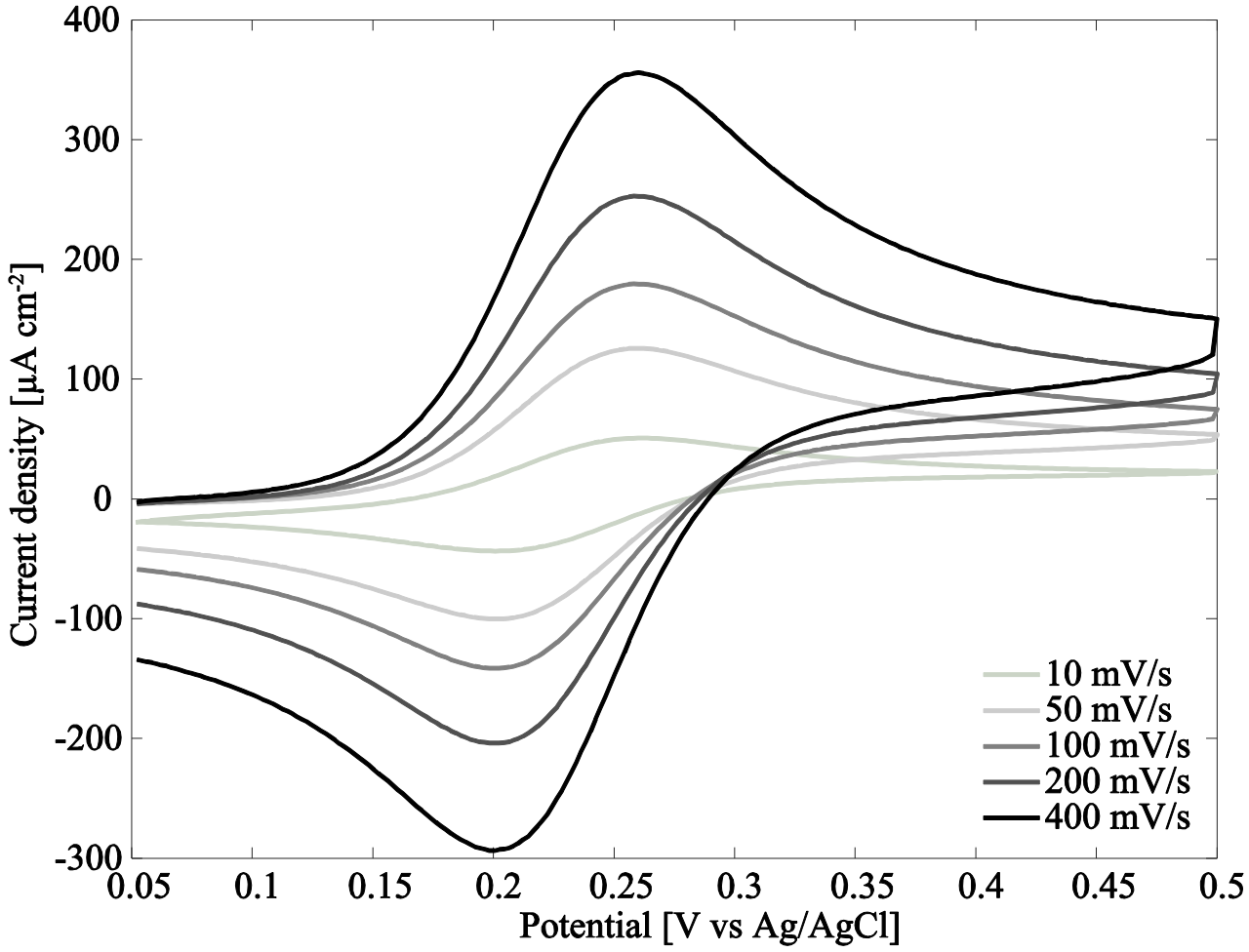

Figure 6. Cathodic (A) and anodic (B) RDE curves for Pt in 0.15 M H_2SO_4 with 1 mM H_2O_2 at scan rate 50 mV/s.

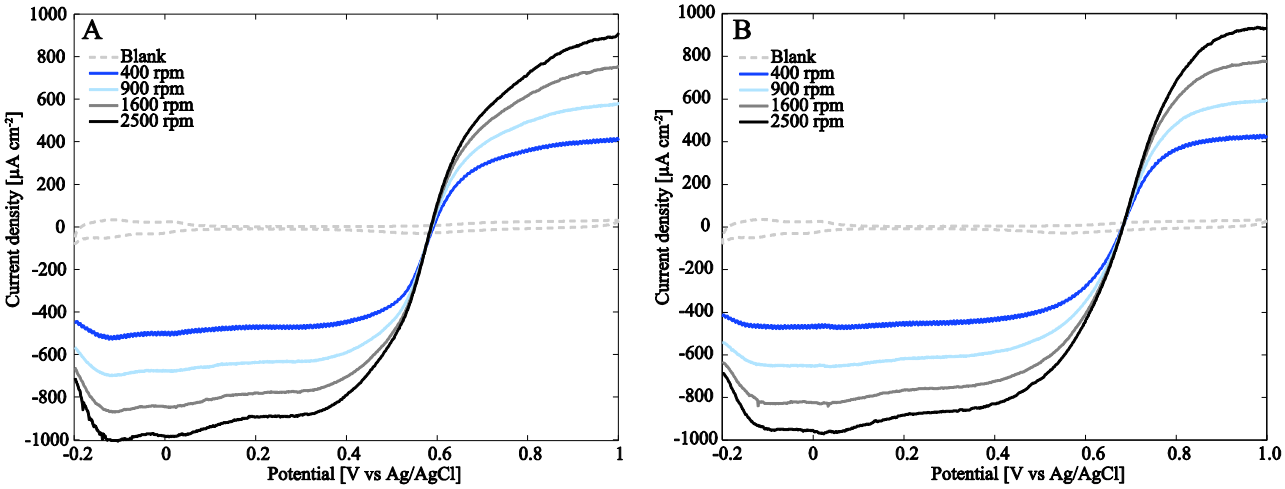

Figure 7. Cathodic (A) and anodic (B) RDE curves for a-C/Pt in 0.15 M H_2SO_4 with 1 mM H_2O_2 at 50 mV/s. Cathodic scan starts from 1 V (vs. Ag/AgCl) and anodic scan from -0.2 V (vs. Ag/AgCl) The dashed lines highlight the shift of the zero current crossing point between anodic and cathodic scans.

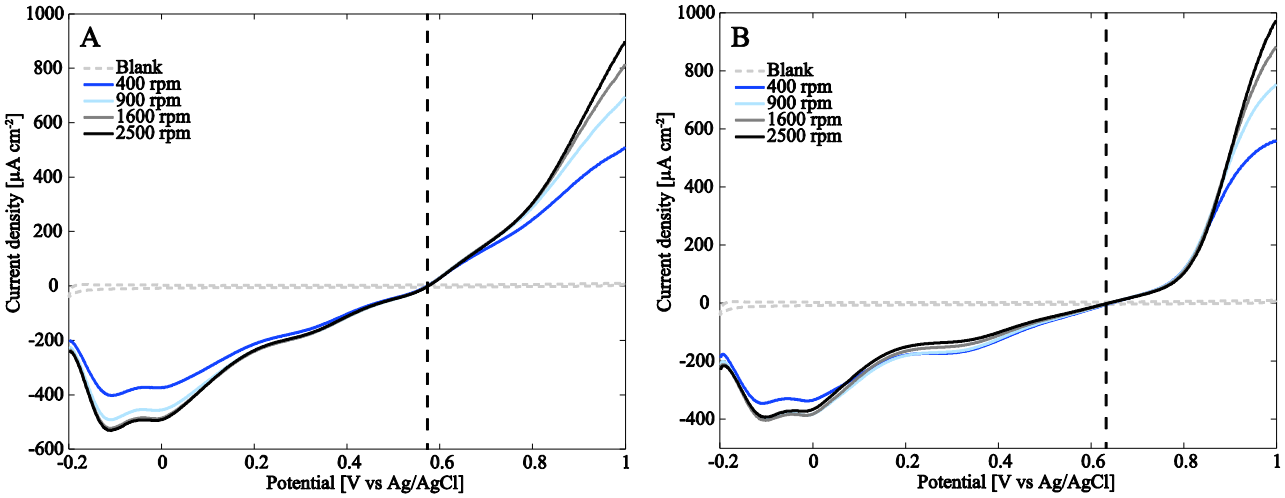

Figure 8. Effect of different upper potential limits 0.4 V and 1.2 V vs. Ag/AgCl (blue and black line, respectively) on OH adsorption in 0.15 M H_2SO_4 (scan rate 50 mV/s). A) a-C/Pt sample shows increase in the current magnitude during the cathodic scan when upper potential limit is increased to region where OH adsorption (i.e. Pt surface oxidation) takes place compared to when there is no OH adsorption. B) For polycrystalline Pt the current magnitude in the cathodic end does not depend on the upper potential limit. This indicates that the strong OH adsorption is characteristic of small islands rather than bulk Pt.

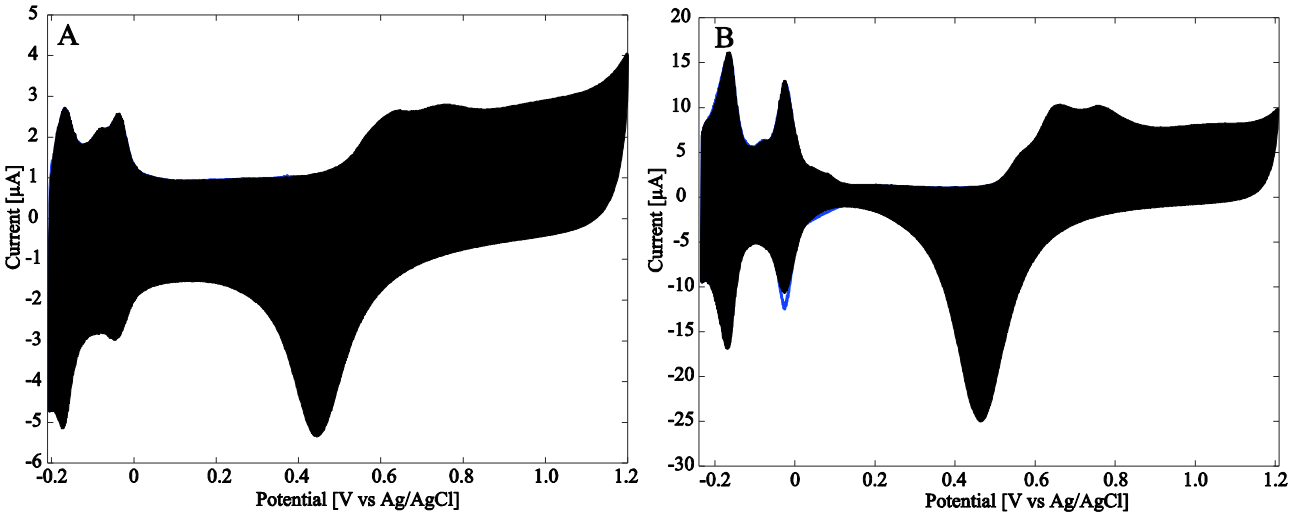

Figure 9. Effect of different upper potential limits 1.0 V and 1.2 V vs. Ag/AgCl (blue and black line, respectively) on CO oxidation in 0.15 M H_2SO_4. A) Stationary cycle after cleaning process using different upper potential limit for samples before CO-stripping experiments at 50 mV/s. B) CO stripping experiments at 20 mV/s for samples with different cleaning protocols. The CO oxidation peak is shifted to anodic direction when there is less extensive cleaning.

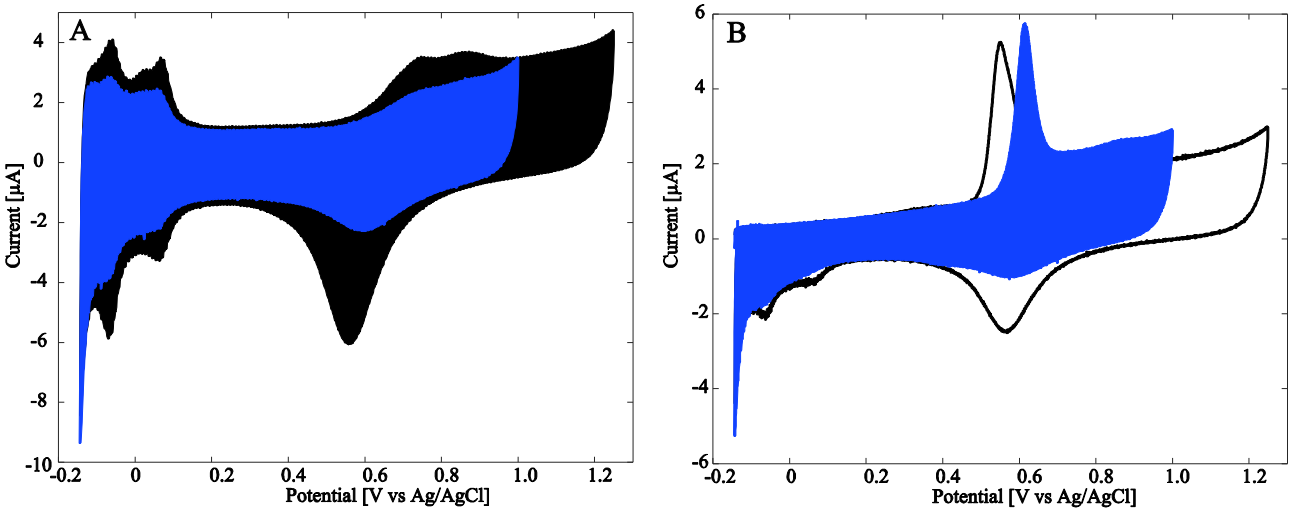

Figure 10. The a-C/Pt samples showed linear behavior in H_2O_2 in PBS between 50 µM and 1000 µM (R^2 = 0.999). Inset shows that the current for 50 µM H_2O_2 deviates clearly from the blank PBS already before 0.05 s.

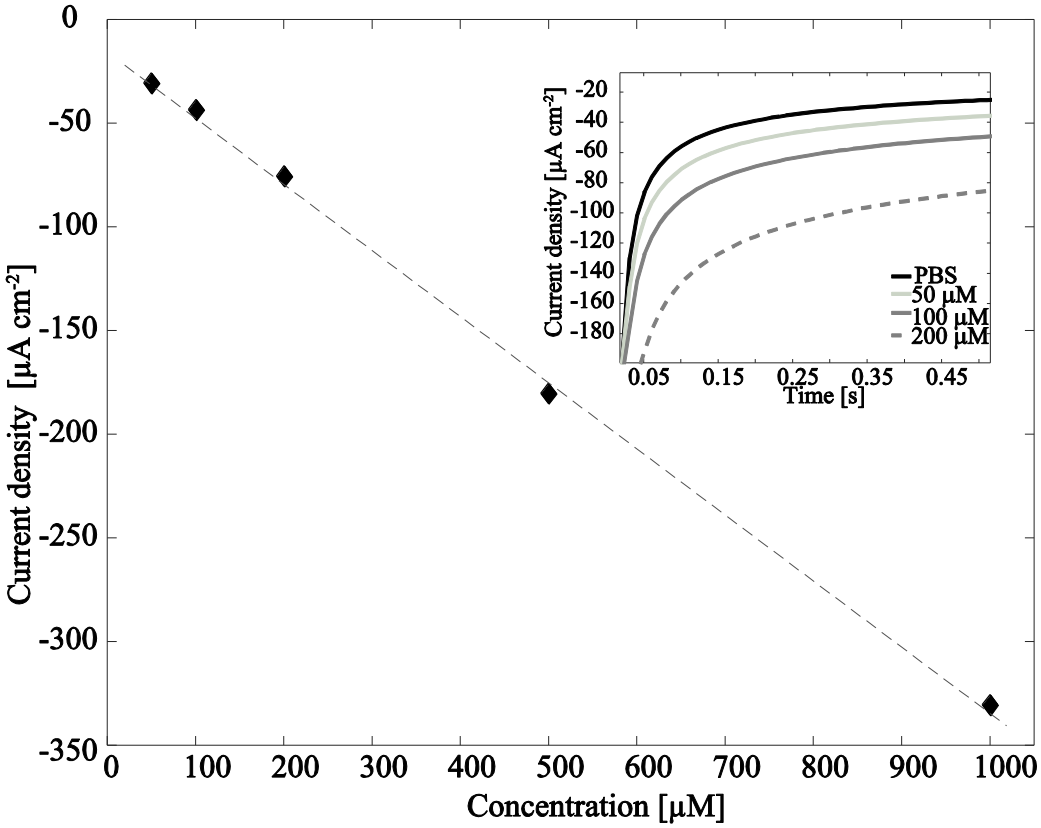

Table 1. Results for a-C/Pt in 1 mM FcMeOH (dissolved in 0.15 M H_2SO_4): peak separations, peak current densities for both oxidation and reduction of FcMeOH, peak current density ratios, and FcMeOH oxidation peak current densities for Pt film.

Scan rate	ΔEp (mV)	$j_{ox,a\text{-}C/Pt}$ (µA cm^{-2})	$j_{red,a\text{-}C/Pt}$ (µA cm^{-2})	$j_{ox,a\text{-}C/Pt}$ /$j_{red,\ a\text{-}C/Pt}$	$j_{ox,\ Pt}$ (µA cm^{-2})
10 mV/s	61.1	41.60	-55.04	0.76	52.10
50 mV/s	60	115.51	-120.38	0.96	120.90
100 mV/s	57.9	161.94	-170.60	0.95	177.17
200 mV/s	57.9	224.98	-238.52	0.94	245.30
400 mV/s	59.7	315.81	-329.62	0.96	344.01